Renewable Energy 201 (2022) 181–193

Contents lists available at ScienceDirect

Renewable Energy

journal homepage: www.elsevier.com/locate/renene

Numerical and experimental study of the hydrodynamic coefficients and power absorption of a two-body point absorber wave energy converter

Amir Rahimi [a,*], Saeed Rezaei [a], Jamshid Parvizian [a], Shahriar Mansourzadeh [b], Jorrid Lund [c], Radhouane Hssini [c], Alexander Düster [c]

[a] Department of Mechanical Engineering, Isfahan University of Technology, Isfahan, 84156-83111, Iran
[b] Research Institute for Subsea Science & Technology, Isfahan University of Technology, Isfahan, 84156-83111, Iran
[c] Institute for Ship Structural Design and Analysis, Hamburg University of Technology (TUHH), Am Schwarzenberg-Campus 4 C, D-21073, Hamburg, Germany

ARTICLE INFO

Keywords:
Wave energy converter
Two-body point absorber
Viscous damping coefficients
Hydrodynamic coefficients

ABSTRACT

This study compares the hydrodynamic coefficients of a two-body point absorber wave energy converter (WEC) model obtained by three methods, namely the experimental method, the finite volume method (FVM), and the boundary element method (BEM). The BEM and FVM numerical simulations of the WEC motion are done using ANSYS AQWA and OpenFOAM, respectively. An experimental method for the accurate calculation of the added mass, damping coefficient, and wave excitation force for the WEC is introduced. The experiments are carried out in a wave tank with a scaled-down WEC model. A comparison of the results shows that – although the BEM is computationally fast, inexpensive, and able to estimate the added mass of the WEC with a reasonable accuracy – it is not able to accurately calculate the damping coefficients. The power absorbed by the WEC is calculated using the hydrodynamic coefficients obtained by all methods. The results show that the viscous damping dramatically decreases the absorbed power. A practical range of dimensionless damping coefficients is proposed to estimate the viscous damping of a two-body point absorber WEC, based on the experimental and FVM results. The upper bound of the absorbed power is also discussed in this paper.

1. Introduction

The fossil fuel crisis and environmental issues have increased the demand for renewable energies. Wave energy is one of the high potential energy resources that attracted many researches over the past two decades [1–4]. Compared to solar energy (0.1–0.3 kW/m^2) and wind energy (0.5 kW/m^2), ocean waves have a potential of 2–3 kW/m^2 [5]. Despite many efforts in the modeling and optimization [6,7], fabrication and testing of laboratory-scaled models [8–13], and development of large-scaled prototypes [14–17], the technology of wave energy conversion is lagged behind other renewable energies in terms of implementation and commercialization [18]. Offshore areas generally exhibit a higher energy density than nearshore regions [19,20]. Hence, it is rather efficient to develop offshore wave energy converters. Among the different types, Point Absorbers (PAs) are the superior type of wave energy converters to be used offshore, due to their simplicity and ability to absorb energy in all directions [3]. PAs, in general, have one (single-body) or two bodies to absorb the energy of the waves, and a power take-off (PTO) system to convert and transmit the absorbed energy. One way to increase the efficiency of the energy absorption is to adapt the natural frequency of the WEC to the wave frequency [21]. In order to achieve this resonance condition at relatively low frequencies of sea waves [20,22], large and massive buoys have to be chosen. However, a practical solution to achieve low natural frequencies for smaller buoys is to add a second body to the PA in order to increase the inertia [23]. By comparing single- and two-body PAs, many studies show the advantages of two-body PAs against single-body PAs in absorbing power at lower frequencies [21,24–26]. The development of two-body PAs requires accurate mathematical modeling to predict and optimize their performances. Falnes [6] developed motion equations of a two-body point absorber by considering a linear PTO system, and obtained optimal PTO parameters to maximize the power absorption. One of the modeling steps is the extraction of hydrodynamic coefficients (the added mass, radiation damping, and wave excitation force) and the viscous drag damping.

Hydrodynamic coefficients can be calculated using the boundary

* Corresponding author.
E-mail address: amir.rahimi@me.iut.ac.ir (A. Rahimi).

https://doi.org/10.1016/j.renene.2022.10.103
Received 14 March 2022; Received in revised form 20 October 2022; Accepted 22 October 2022
Available online 26 October 2022
0960-1481/© 2022 Elsevier Ltd. All rights reserved.

element method (BEM) based on the linear wave theory [27]. As the BEM discretizes the equations of inviscid fluid, the viscous effect is not considered when calculating the hydrodynamic coefficients. Ignoring viscous effects can lead to an overestimating of the absorbed power [25,26]. Beatty et al. [26,28] extracted hydrodynamic coefficients of two different submerged body geometries, namely Powerbuoy [29] and Wavebob [15], using the experimental method. They compared the results with the corresponding results obtained by the BEM. They concluded that the damping coefficients obtained by the experimental method are much larger than those obtained by the BEM. Liang et al. [25] established a linear relationship for estimating the viscous damping using a dimensionless coefficient. They provided the values of dimensionless coefficients for the submerged body of Powerbuoy and Wavebob using the experimental data presented in Ref. [26]. To obtain more accurate results and analyze the viscous effects on the hydrodynamics coefficients, it is necessary to employ computational fluid dynamic (CFD) simulations in which the Navier-Stokes equations are solved. To estimate the modeling error due to the boundary conditions, the turbulence model, etc. in the CFD simulations, the results must be validated by experiments. Once the numerical results are validated with the experiments, the CFD simulations can be used as a replacement for the expensive experiments.

Jin et al. [30] investigated the viscous effect on the power absorption efficiency and the hydrodynamic performance of a 1:50 scale heave oscillating single-body point absorber. They compared the experimental results for a linear state-space model (LSSM) and a non-linear state-space model (NSSM) with corresponding results obtained by CFD. They concluded that the conventional LSSM fails to predict the power absorption efficiency and the hydrodynamic performance accurately, especially near the resonance frequency or at high wave heights. Chen et al. [31] studied the viscous effect of single-body heave PA WECs with cylindrical floaters for different bottom shapes using the free decay test – and developed a viscous correction formula based on the ratio of the diameter to draft, as an independent variable. Al Shami et al. [32] presented CFD simulations for different shapes of the submerged body of a two-body point absorber in a three-dimensional non-linear numerical wave tank (NWT) and calculated viscous drag coefficients. Further, they investigated the effects of the viscous drag damping on the power absorption and concluded that the cylindrical submerged body performs best in low wave frequencies (0.05–0.1 Hz), the spherical submerged body performs best in medium wave frequencies (0.1–0.119 Hz), and the ellipsoidal submerged body performs best in high wave frequencies (0.119–0.137 Hz).

In this paper, the energy absorption capacity of a two-body point absorber wave energy converter (2B-PA WEC) is investigated for the case of the WEC's interaction with regular waves. If the PTO system is modeled by a spring-damper system, the energy absorbed in a given WEC, at each wave frequency, depends on the damping and stiffness coefficients of the PTO system. At a specific damping and stiffness coefficient, the maximum energy can be harvested with a WEC. Therefore, by determining these coefficients in each frequency and adjusting the PTO accordingly, the maximum power can be extracted from the WEC. To evaluate the maximum power output at different frequencies, a 2B-PA WEC model is developed and tested in a wave tank. The general shape of the WEC model is chosen similar to the Powerbuoy PB500 (scale 1:23). However, its dimensions are those recommended in Ref. [33] following an optimization procedure using design of experiments (DoE) and response surface method (RSM) developed by the current authors. Fig. 1 shows the geometry of the fabricated WEC. The WEC consists of a floating buoy and a submerged body which, due to their interactions with the wave, oscillate relative to each other in the vertical direction.

To determine the amount of the absorbed power, it is necessary to calculate the hydrodynamic coefficients (added mass and damping coefficients), the hydrostatic coefficient of the bodies, and the wave excitation force. This paper compares three approaches to determine

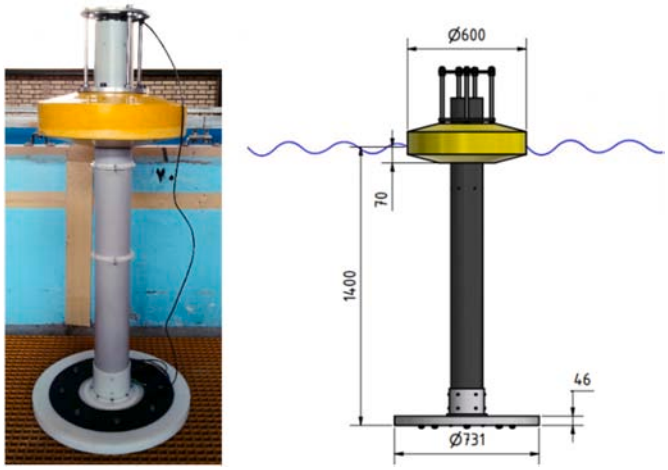

Fig. 1. Fabricated WEC (left) and its dimensions in mm (right).

these coefficients: the boundary element method (BEM) using the ANSYS-AQWA software [34], the finite volume method (FVM) using the OpenFOAM software [35], and an experimental method. Each approach is described in detail in Section 3. The comparison helps to validate the approaches and select a fast, robust, and low-cost method for this purpose. Section 4 presents and compares the obtained results as well as the absorbed power based on data for each of the methods. Section 5 concludes the paper.

2. Mathematical modeling

WECs are mainly subjected to wave forces, hydrodynamic forces, hydrostatic restoring forces, and the load induced by the PTO system. A mathematical model should include dynamic and hydrodynamic forces to address the behavior of a WEC.

2.1. Motion equations

In general, WECs can have six degrees of freedom (DoF) in response to the external forces. For PAs, however, depending on the type of absorber, only the linear motion in heave or the rotation in pitch are considered. A 2B-PA can be modeled as a 2-DoF mass-spring-damper system, see Fig. 2. The equation of motion for a heave-constrained 2B-PA in the frequency domain – considering the linear PTO system – can be given as [6]:

$$Z(\omega)[\widehat{U}_1\ \widehat{U}_2]^T = \begin{bmatrix} Z_1 + Z_{PTO} & -Z_{PTO} \\ -Z_{PTO} & Z_2 + Z_{PTO} \end{bmatrix} [\widehat{U}_1\ \widehat{U}_2]^T = [\widehat{F}_{e_1}\ \widehat{F}_{e_2}]^T \tag{1}$$

where subscripts 1 and 2 refer to the parameters of the floating and submerged bodies, respectively. $\widehat{U}_j$ is the complex amplitude of each body velocity, $\widehat{F}_{e_j} = A_w F_{e_j} e^{i\varphi}$ is the complex wave excitation force in which F_{e_j} is the normalized amplitude of the wave excitation force, A_w is the amplitude of the incident wave, and φ is the phase difference between the wave excitation force and wave elevation. $Z(\omega)$ is the complex mechanical impedance matrix, in which:

$$Z_1 = \left(B_1 + b_{vis1}\right) + i\omega\left((m_1 + A_1) + r \bullet m_{PTO} - \frac{K_{s1}}{\omega^2}\right) \tag{2}$$

$$Z_2 = (B_2 + b_{vis2}) + i\omega\left((m_2 + A_2) + (1 - r)m_{PTO} - \frac{K_{s2}}{\omega^2}\right) \tag{3}$$

where i is the imaginary unit, B_j and b_{vis_j} are the radiation and viscous damping coefficients, respectively, m_j is the mass and A_j is the added mass of each body, m_{PTO} is the mass of the PTO and r is the fraction of

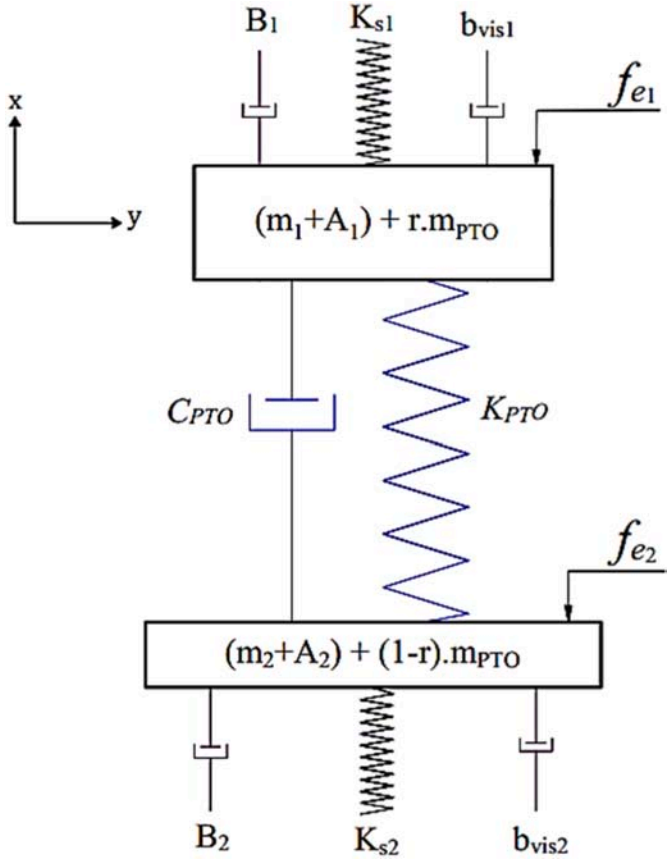

Fig. 2. Mass-spring-damper model of a 2B-WEC.

PTO mass contributing to the floating buoy, K_{s_j} is the hydrostatic stiffness, and ω [rad /s] is the wave frequency. Z_{PTO} is the complex mechanical impedance induced by the load of the PTO. For a linear system, Z_{PTO} is given as:

$$Z_{PTO} = C_{PTO} - i\omega\frac{K_{PTO}}{\omega^2} \tag{4}$$

where C_{PTO} and K_{PTO} are the damping and stiffness coefficients of the PTO, respectively.

From Eq. (1), the relative velocity of the floating buoy and the submerged body can be obtained as:

$$\widehat{U}_{rel} = \widehat{U}_1 - \widehat{U}_2 = \frac{\frac{\widehat{F}_{e1}Z_2 - \widehat{F}_{e2}Z_1}{(Z_1+Z_2)}}{\frac{Z_1Z_2}{(Z_1+Z_2)} + Z_{PTO}} = \frac{\widehat{F}_{eq}}{Z_{eq}+Z_{PTO}} \tag{5}$$

where $\widehat{F}_{eq}$ and Z_{eq} are the equivalent wave excitation force and the equivalent complex mechanical impedance matrix, respectively, defined as:

$$\widehat{F}_{eq} = \frac{\widehat{F}_{e1}Z_2 - \widehat{F}_{e2}Z_1}{(Z_1+Z_2)} \tag{6}$$

$$Z_{eq} = \frac{Z_1Z_2}{(Z_1+Z_2)} \tag{7}$$

2.2. Power absorption

The time-averaged value of mechanical absorbed power, $\overline{p_u(t)}$, can be determined by multiplying the PTO force by the relative velocity of the two bodies [6]:

$$P_u \equiv \overline{p_u(t)} = \overline{f_{PTO}(t) \bullet u_{rel}(t)} = \frac{1}{2}C_{PTO}|\widehat{U}_{rel}|^2 \tag{8}$$

By substituting Eq. (5) into Eq. (8), the time-averaged mechanical absorbed power can be obtained as:

$$P_u = \frac{1}{2}C_{PTO}\left|\frac{\widehat{F}_{eq}}{(C_{PTO}+Re\{Z_{eq}\}) + i\left(Im\{Z_{eq}\} - \frac{K_{PTO}}{\omega}\right)}\right|^2 \tag{9}$$

To achieve the maximum averaged power, two control strategies can be followed [5]. In the first strategy, to maximize the mechanical absorbed power, the partial derivative of the absorbed power with respect to C_{PTO} is taken and set equal to zero, i.e.

$$\frac{\partial P_u}{\partial C_{PTO}} = 0 \tag{10}$$

This strategy, known as *amplitude control,* leads to the following equation [33]:

$$C_{PTO_{opt}} = \sqrt{\left(Re\{Z_{eq}\}\right)^2 + \left(Im\{Z_{eq}\} - \frac{K_{PTO}}{\omega}\right)^2} \tag{11}$$

The second strategy minimizes the denominator of Eq. (9) by eliminating its imaginary part, i.e.:

$$Im\{Z_{eq}\} - \frac{K_{PTO}}{\omega} = 0 \tag{12}$$

This makes the wave excitation force and the relative velocity of the two bodies act in the same phase. Then, the optimum stiffness of the PTO can be determined from Eq. (13). This strategy is known as *complex-conjugate control* [5]

$$K_{PTO_{opt}} = \omega Im\{Z_{eq}\} \tag{13}$$

Considering Eqs. (11) and (13) simultaneously, the optimum PTO damping, the optimum relative velocity, and its corresponding maximum averaged power can be obtained as Eqs. (14) to (16):

$$C_{PTO_{opt}} = Re\{Z_{eq}\} \tag{14}$$

$$\widehat{U}_{rel_{opt}} = \frac{\widehat{F}_{eq}}{2Re\{Z_{eq}\}} \tag{15}$$

$$P_{u_{opt}} = \frac{|F_{eq}|^2}{8Re\{Z_{eq}\}} \tag{16}$$

If at a certain wave frequency a negative value is obtained for K_{PTO}, its magnitude is considered to be zero, since a negative spring coefficient is not practically meaningful. In the case of $K_{PTO} = 0$, the PTO impedance is restricted to be real ($Z_{PTO} = C_{PTO}$). In this case, a passive control is applied [25,26] and the absorbed power will be suboptimal. The suboptimum PTO damping coefficient that maximizes the averaged absorbed power can be written as:

$$C_{PTO_{subopt}} = |Z_{eq}| \tag{17}$$

The suboptimum relative velocity and the maximum averaged absorbed power are given by Eqs. (18) and (19) respectively:

$$\widehat{U}_{rel_{subopt}} = \frac{\widehat{F}_{eq}}{Z_{eq} + |Z_{eq}|} \tag{18}$$

$$P_{u_{subopt}} = \frac{|F_{eq}|^2}{4\left(Re\{Z_{eq}\} + |Z_{eq}|\right)} \tag{19}$$

2.3. Upper bound on power absorption

There are different ways to increase the PAs output power such as optimizing the PTO parameters. However, the power increase is limited to an upper bound value. This section tries to obtain an upper bound on the absorbed power. Budal's theory is used to predict the maximum available power that can be extracted from the wave excitation force [5, 26]. The theory assumes that a PA oscillates in optimal conditions and operates at the maximum relative velocity. Based on Falnes [6], the available time-averaged captured power for a single-body PA is obtained as

$$P_a = \overline{f_e(t)u(t)} = \frac{1}{2}|\widehat{F}_e||\widehat{U}|cos\ (\gamma) \tag{20}$$

where γ is the phase difference between the body's relative velocity and wave excitation force. Using an equivalent wave excitation force ($\widehat{F}_{eq}$) and relative velocity ($\widehat{U}_{rel}$) for a two-body PA, the available time-averaged captured power for a 2B-PA can be written as

$$P_a = \frac{1}{2}|\widehat{F}_{eq}||\widehat{U}_{rel}|cos\ (\gamma_r) \tag{21}$$

in which $\widehat{F}_{eq}$ is the net force applied to the WEC by the wave, when two bodies of the WEC are connected to each other and they form a single body i.e. $Z_{PTO} = \infty$.

The Budal's upper bound for the maximum absorbed power (P_{a-Max}) uses two assumptions: (i) the relative velocity and the equivalent wave excitation force are in the same phase, i.e. $\gamma_r = 0$, and (ii) the maximum relative velocity $\widehat{U}_{relmax}$ is achieved. Considering these two assumptions, the inequality of power capture can be obtained as:

$$P_u \le P_a \le \frac{1}{2}|\widehat{F}_{eq}||\widehat{U}_{relmax}| \tag{22}$$

The relative velocity, at each frequency, reaches its maximum value if any of the two following cases occurs, (i) the control parameter Z_{PTO} in Eq. (4) is set to zero, or (ii) the maximum stroke of the PTO is achieved. The first case implies that the two bodies move independently. That is, the PTO has no resistance against the movement of the bodies relative to each other. Although this is practically impossible, it provides an estimate for the maximum relative velocity:

$$\widehat{U}_{rel_{max}} = \frac{\widehat{F}_{eq}}{Z_{eq}} \tag{23}$$

The second case implies that the maximum relative velocity is given as:

$$\widehat{U}_{rel_{max}} = \omega s_{max} \tag{24}$$

where s_{max} is the maximum stroke of the PTO.

The upper bound of the absorbed power can be obtained by replacing Eqs. (23) and (24) into Eq. (22):

$$P_u \le P_a \le \frac{\widehat{F}_{eq}^2}{2|Z_{eq}|} \tag{25}$$

$$P_u \le P_a \le \frac{1}{2}|\widehat{F}_{eq}|\ \omega s_{max} \tag{26}$$

3. Power calculation

In the motion equations, Eqs. (1)–(3), A_j, B_j, and $\widehat{F}_{e_j}$ are functions of frequency. To calculate the power absorbed by the WEC at each frequency, the following calculations must take place in this order:

1 the added mass and damping coefficient together with the exciting force of two buoys,
2 the impedance values, Z_1, Z_2, and Z_{eq} from Eqs. (2), (3) and (7) respectively,
3 $\widehat{F}_{eq}$ from Eq. (6),
4 the absorbed power $P_{u\,subopt}$ by the WEC from Eq. (19).

As can be seen, calculating the hydrodynamic coefficients is the first step in estimating the power absorbed by the WEC. In addition, the accuracy of the calculation of the absorbed power in each frequency depends on the accuracy of the calculated added masses, damping coefficients, and wave excitation forces obtained in the first step. Therefore, it is very important to calculate these parameters with high accuracy. In this paper, we present a novel experimental method for the accurate measurement of added masses, damping coefficients, and excitation force of the buoys. The values obtained with this method are compared with corresponding values obtained by ANSYS-AQWA, which solves the potential flow theory (inviscid flow) using the BEM, and OpenFOAM software which solves the Reynolds averaged Navier–Stokes equations (RANS) with the FVM. The absorbed power will be calculated and compared using parameters obtained by all three different methods. These procedures are explained in the following sections.

3.1. Calculation of hydrodynamic coefficients

This section serves to describe the methods used in the current study to calculate the added mass, the damping coefficient, and the wave excitation. The results obtained from these methods are presented in Section 4.

3.1.1. BEM

In this section, the ANSYS-AQWA software is used to calculate the added mass, the radiation damping, and the wave excitation force by applying the BEM. ANSYS-AQWA uses the potential flow theory, assuming an inviscid, incompressible, and irrotational flow. Drawing on the velocity potential and a diffraction/radiation theory, one can write:

$$u = \nabla \Phi \tag{27}$$

$$\Phi(x.t) = \Phi_I + \Phi_D + \Phi_R \tag{28}$$

in which Φ_I is the undisturbed incident wave potential, Φ_D is the diffraction potential surrounding a restrained body, and Φ_R is the radiation potential generated by an oscillating motion of a body in still water. In the diffraction theory, the potential function is calculated by solving the Laplace equation, applying appropriate boundary conditions, and then calculating the pressure and forces acting on the body. These parameters will be used to calculate the added masses and damping coefficients.

3.1.2. FVM

This section focuses on the development of the numerical fluid simulation to extract the added mass and the damping coefficients. The radiation test, which will be described in Section 3.1.3.1, is numerically simulated using OpenFOAM, an open-source CFD code. For this purpose, a sinusoidal heave movement with a predefined amplitude range between 1 and 5 cm is used. In total, ten frequencies in the range of 0.1–1 Hz are tested for both floating and submerged bodies. The damping and added mass are extracted based on the calculation of the amplitude of the heave force, F, and the phase difference between the heave force and displacement, φ. The fluid domain is discretized with the FVM. The WEC is modeled as a rigid body moving inside the fluid domain. The volume of fluid (VOF) method is used to model the two-phase flow [36]. The RANS equations are used with a $k-\varepsilon$ turbulence model to account for turbulent effects. To reduce the simulation time, the domain is divided into 2 inner fine mesh blocks and 34 outer coarse mesh blocks. The buoys geometries are located in the inner blocks. The inserted geometries in the discretized numerical wave tank (NWT) are shown in Fig. 3.

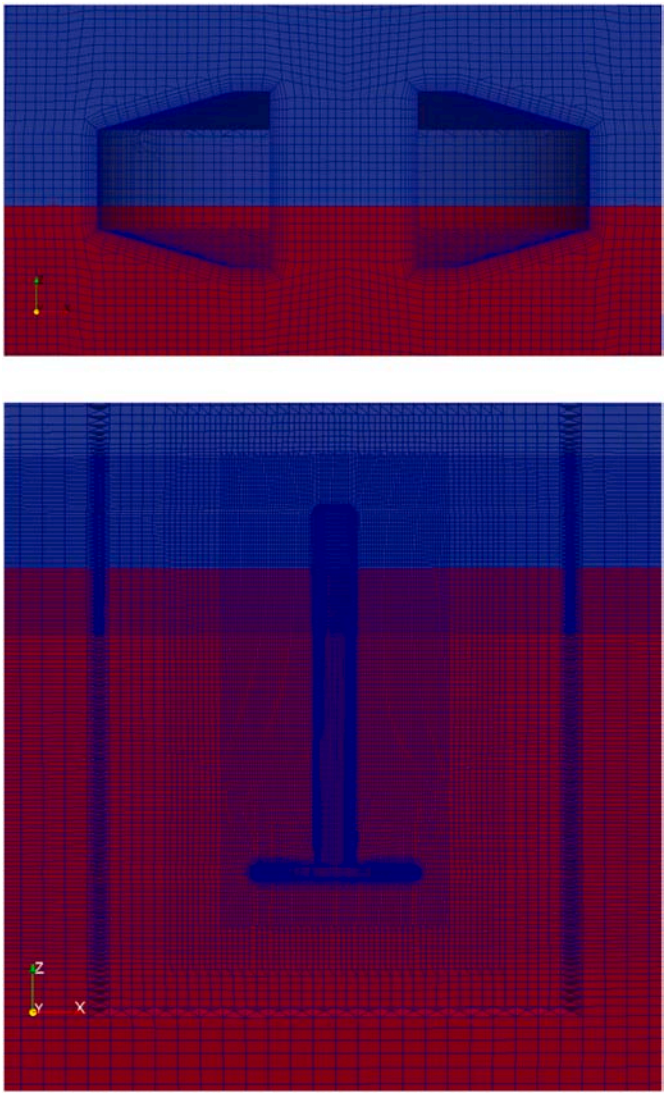

Fig. 3. Details of OpenFOAM mesh structure.

In order to verify the FVM results, similar simulations were carried out using Ansys-CFX. Describing the details of simulation conditions is out of scope of this paper, However, more details including simulation domain, governing equations, mesh study, boundary conditions, convergence criteria, etc. can be found in Refs. [37,38]. The results of the simulations obtained by OpenFOAM are presented in Section 4.

3.1.3. Experimental method

The experiments carried out to calculate the hydrodynamic coefficients consist of a radiation test, a diffraction test, and an upper bound test. Details of these experiments are described in the following sections.

3.1.3.1. Radiation test. In this study, an experimental method known as the radiation test is used to measure the added masses and damping coefficients of the floating and submerged bodies. In this method, the oscillatory motion of each buoy in still water is modeled with the motion of a mass-spring-damper system subjected to an external force, as depicted in Fig. 4.

The equation of motion of the system can be written as:

$$(A+m)\ddot{x}(t)+c\dot{x}(t)+kx(t)=f(t) \tag{29}$$

where, m is the mass of the buoy, A is the added mass representing the

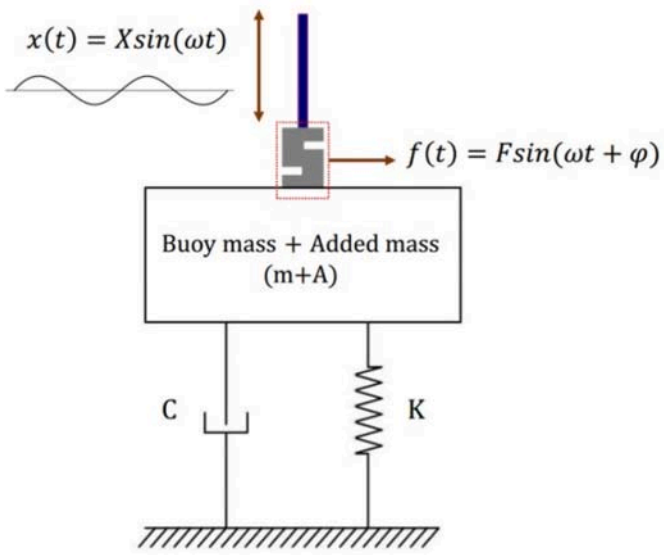

Fig. 4. Mass-spring-damper model of an oscillating buoy in still water.

mass of water accelerated as a result of the buoy movement, c is the sum of radiation and viscous damping coefficient, and k is the spring stiffness representing the changes in the buoyancy force as a result of the buoy motion. To measure the added mass and damping coefficient of the buoy, one can apply a sinusoidal motion with amplitude X and frequency ω to the buoy:

$$x(t)=Xsin(\omega t) \tag{30}$$

The velocity and acceleration of the buoy, then, can be obtained as:

$$\dot{x}(t)=X\omega\ cos\ (\omega t) \tag{31}$$

$$\ddot{x}(t)=-X\omega^2\ sin\ (\omega t) \tag{32}$$

To apply a sinusoidal motion, a sinusoidal external force should be applied to the mass. The sinusoidal force has a phase difference of φ with the displacement, i.e.

$$f(t)=Fsin(\omega t+\varphi) \tag{33}$$

By substituting Eqs. 30–33 into Eq. (29) and rearranging, one obtains:

$$\{-(A+m)\omega^2+k\}Xsin(\omega t)+cX\omega\ cos\ (\omega t)=Fcos(\varphi)sin(\omega t) + Fsin\ (\varphi)cos(\omega t) \tag{34}$$

Equating the coefficients of sine and cosine expressions on both sides of the above equation results in:

$$A+m=\frac{1}{\omega^2}\left(k-\frac{Fcos(\varphi)}{X}\right) \tag{35}$$

$$c=\frac{Fsin(\varphi)}{\omega X} \tag{36}$$

By measuring the applied force, $f(t)$, and calculating its maximum value, F, and the phase difference between the force and displacement, φ, the added mass and damping coefficient can be calculated using Eqs. (35) and (36) respectively.

3.1.3.2. Diffraction test. To experimentally measure the wave excitation force applied on each buoy (mass), the buoy must be kept stationary in its equilibrium condition, in which the buoyancy force and the weight of the buoy are equal. If the buoy is hit by an incident wave – with a certain height and frequency – a load cell can be used to measure the vertical force, which is equal to the wave exciting force (Fig. 5). The force, then,

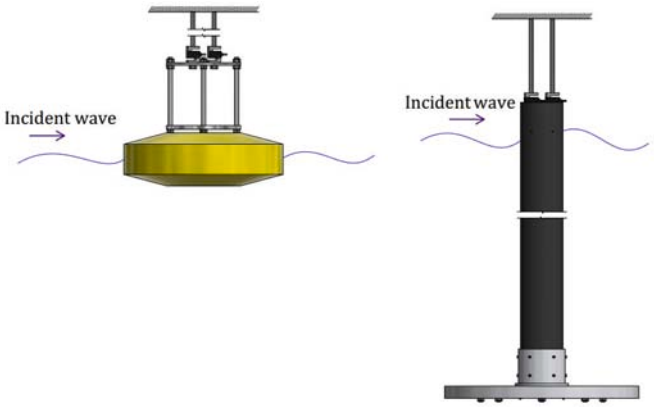

Fig. 5. Diffraction test model.

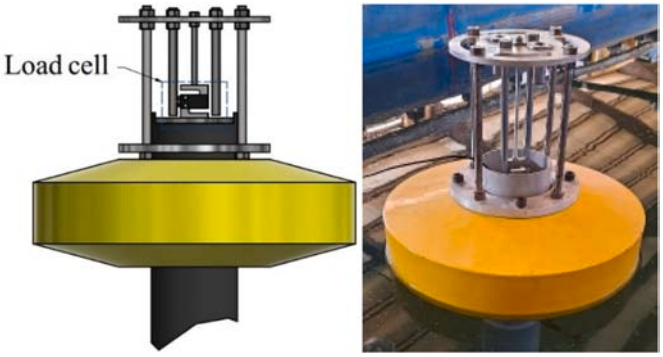

Fig. 6. Upper bound test (maximum net absorbed force).

can be normalized by the wave height η.

3.1.3.3. Upper bound test. To calculate the upper bound power by the experimental method, according to Eqs. (25) and (26), it is necessary to measure the maximum relative velocity of the bodies and the net force applied by the incident wave on two bodies when connected to each other. The test is carried out in two steps: in the first step, to measure the net wave force $\widehat{F}_{eq}$, floating and submerged bodies are connected to each other through a tension-pressure S-type load cell (as shown in Fig. 6). Using the load cell, the time-dependent force applied by the regular wave on the connected bodies is measured and recorded. At each frequency, the amplitude of the time-dependent force $\widehat{F}_{eq}$ is determined. In the second step, to calculate the maximum relative velocity, the two bodies are allowed to oscillate with regular waves relative to each other, while the PTO is disconnected, see Fig. 7. The relative displacement of two bodies is measured by a laser displacement sensor. The maximum relative velocity can be calculated by multiplying the relative displacement (S_{max}) by the wave frequency (ω).

3.2. Experimental setup

A wave tank with a length of 110 m, a width of 3 m, and a depth of 2.2 m is used to perform the experiments. A wedge-type wave maker is used to create regular waves in the frequency range of 0.1–1 Hz, with a maximum wave height of 0.2 m. A wave absorber, basically consisting of four adjustable inclined perforated plates, is installed at the end of the wave tank to prevent the incident wave from reflecting back. To ensure that the wave does not reflect back, several wave sensors are installed along the tank and monitor the wave specification. The stability of the generated wave during the test indicates the absence of any significant reflected wave. In addition, the wave absorber, shown in Fig. 8, includes 4 perforated plates with different levels of perforations. The angle of perforated plates, as well as, the level of their insertion inside the water tank is adjustable. Several experiments are already carried out using different angles of perforated plates in various level of insertion inside the tank, at different periods and wave amplitudes, to ensure minimum reflection of the generated wave. In order to minimize the effect of the wave reflection from the lateral walls of the wave tank, the outer diameter of the floating buoy is selected to be 0.6 m, i.e., about 1/5 of the wave tank width. To measure the wave height, four wave gauges (Akamina AWP-24-SP) are used. Fig. 8 shows a schematic of the experimental setup. The operation of the WEC inside the wave tank can be observed in: https://subseard.iut.ac.ir/sites/subseard/files/Site/wec in the pool_3.mp4.

3.2.1. Vertical oscillating mechanism

In order to experimentally measure the added mass and damping coefficients of the float and submerged bodies of the WEC, with the theoretical method described in Section 3.1.3.1, a vertical oscillating mechanism (VOM) is designed and fabricated, see Fig. 9. It uses a 1000 Watt AC servo motor to create a rotational motion. A system consisting of a ball screw and a linear guide converts the rotational motion into a sinusoidal oscillating motion. The operating frequency range of the system is 0–1.5 Hz, and the maximum oscillation height is 15 cm. To set

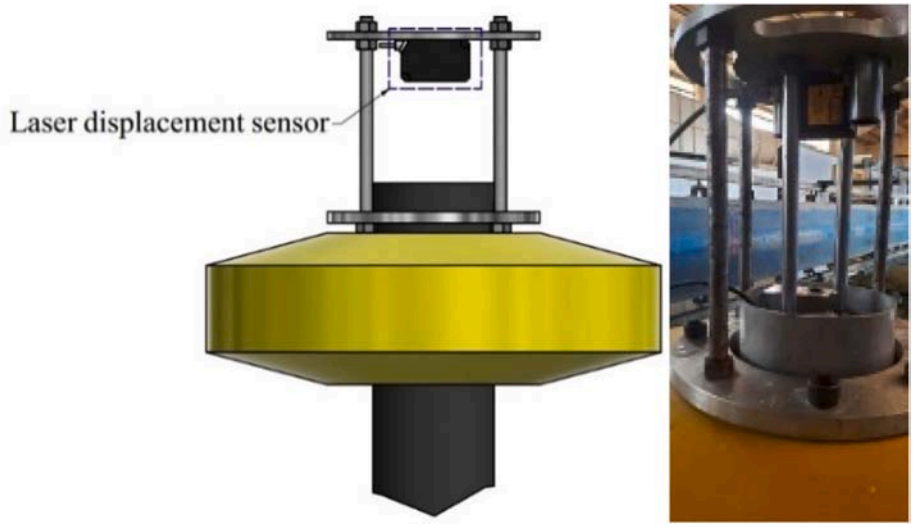

Fig. 7. Upper bound test (maximum relative velocity).

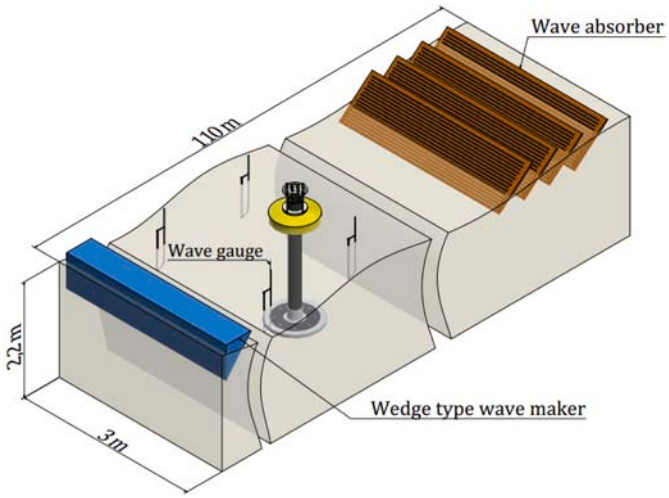

Fig. 8. Schematic of experimental setup and wave tank dimensions.

the operating parameters, a graphical user interface (GUI) is developed in NI LabVIEW software [39].The GUI and part of the LabVIEW block diagram is shown in Appendix A. Using this interface, a sine motion command is sent to the programmable logic controller (PLC) by specifying the amplitude and frequency of the oscillation. Finally, the motion signal is sent to the servo drive and, based on the received command, the servo motor generates the desired rotational motion. A laser displacement sensor (Baumer OM30-P0350.HV.TXN) is used to measure the vertical displacement. The forces applied on the buoys are measured using two 50 kg S-type load cells (ZEMIC H3–C3-50kg-6B-D55). Fig. 10 illustrates the operating principle of the VOM. Fig. 11 shows how the floating and submerged bodies of the WEC are connected to the VOM through two load cells during the experiments. The VOM system is used to run all the experiments discussed in Section 3.1.3.1. The experiments are carried out in the frequency range of 0.1–1 Hz, with a step size of 0.1 Hz.

4. Results

In this section, the experimental results for determining the hydrodynamic coefficients of each body are presented and compared to the hydrodynamic coefficients obtained by the BEM and FVM methods.

4.1. Radiation test

As described in Section 3, the added masses of the floating and submerged bodies are measured both by experimental and numerical methods in the frequency range of 0.1–1 Hz. The results are shown in Fig. 12. The added mass is calculated experimentally for oscillating heights of 2 and 4 cm for the floating body, and for the oscillating heights of 2, 4, and 6 cm for the submerged body. The added masses obtained by the experimental method are determined several times at each frequency. The standard deviation of the results is shown in Fig. 12. The figure also shows the added masses calculated by the BEM (ANSYS-AQWA) and FVM (OpenFOAM). For both the floating and the submerged bodies, the experimental results show that the added mass does not change significantly with the vertical oscillation height.

The added mass is also not a strong function of the frequency. These results agree well with those obtained by Ref. [40]. Further, the results show that the added masses obtained by the experimental method, for the submerged body, agree well with those obtained by the BEM. The added masses obtained for the floating buoy by the experimental method is also consistent with those extracted by the BEM and FVM at frequencies larger than 0.3 Hz. However, there are big discrepancies between the values obtained at lower frequencies. This is due to the fact that the added mass is sensitive to the measured forces at low frequencies.

To investigate the sensitivity of the added mass to the wave fre-

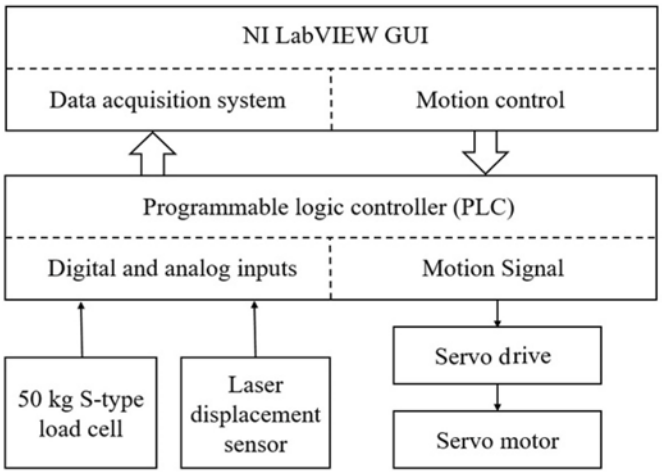

Fig. 10. The operation principle of the VOM.

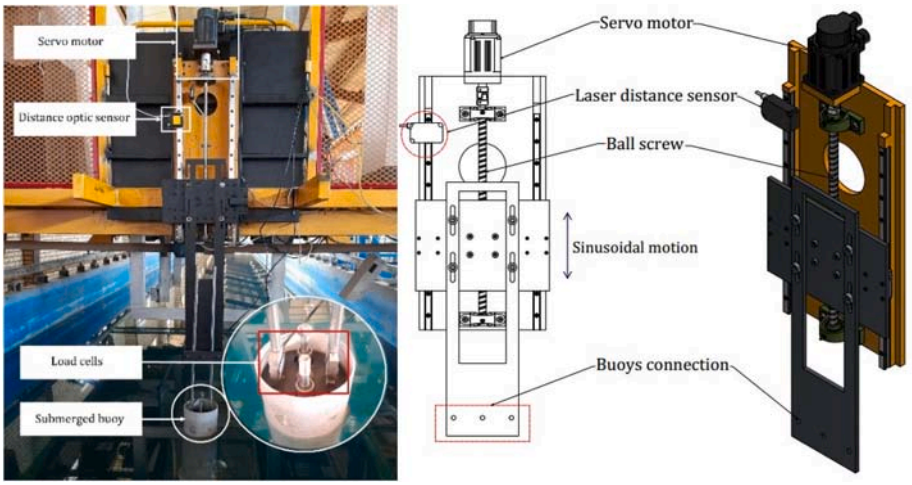

Fig. 9. Vertical oscillating mechanism.

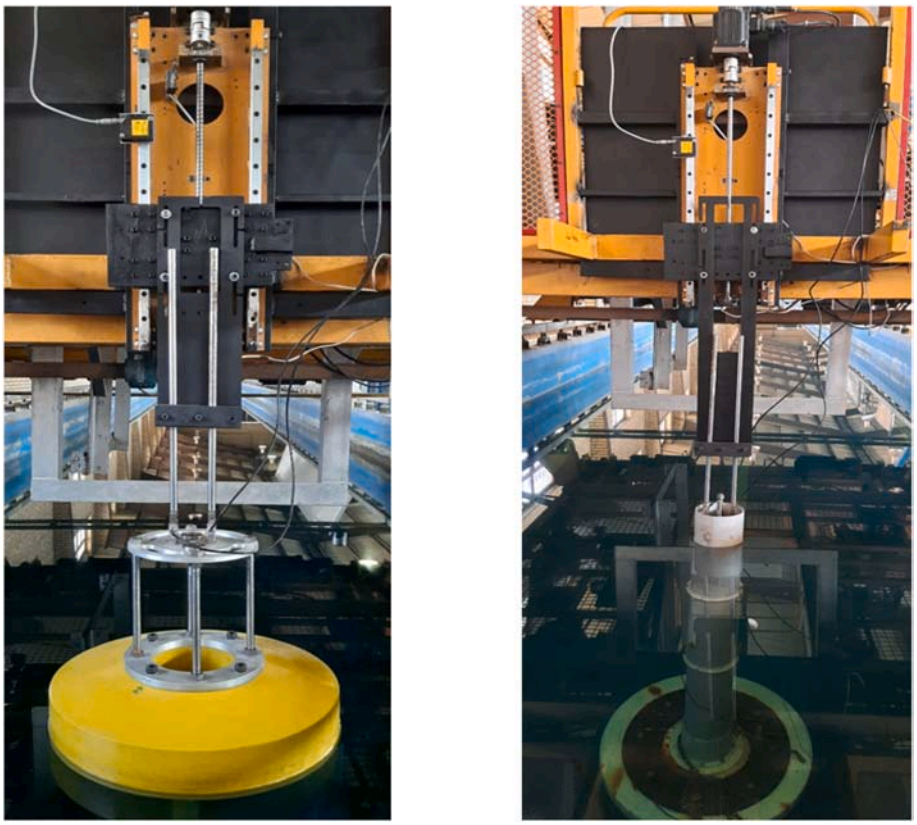

Fig. 11. Connection of the floating and submerged bodies to the vertical oscillating mechanism.

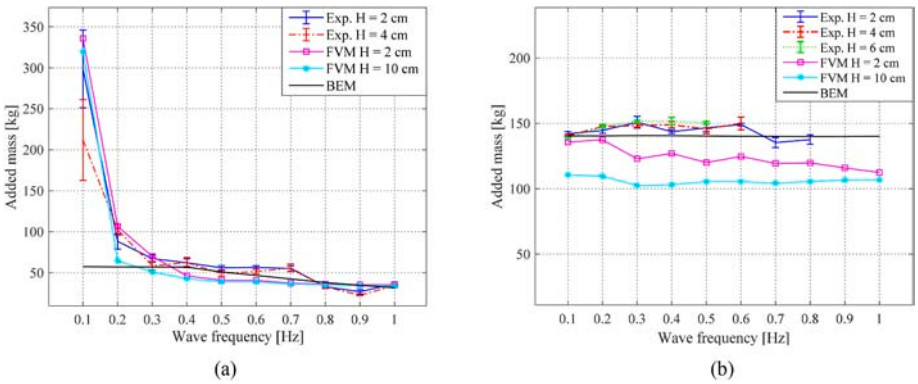

Fig. 12. Added mass obtained from different methods for (a) floating buoy and (b) submerged body. (Vertical lines in the experimental results indicate the standard deviation of the experiments.)

quency, the partial derivative of Eq. (35) with respect to the force is taken:

$$\left|\frac{\partial(A+m)}{\partial F}\right| = \frac{\cos(\varphi)}{\omega^2 X} \tag{37}$$

This equation indicates that the variation of the added mass with respect to the measured force increases sharply as the frequency decreases to low values. In other words, the added mass is highly sensitive to the measured force at low frequencies. Therefore, at low frequencies, a small variation in measuring the force results in a large variation in the calculated added mass. Therefore, if an experiment is repeated twice, even a small difference between the measured forces will result in a large difference between the calculated added masses. This explains why the standard deviation of the added mass is very large at low frequencies for the floating body. Disturbances created by the floating body at the water surface cause large disturbances in the measured forces. For the submerged body, because of the low interaction with the surface water, the measured force does not change significantly if the experiment is repeated.

Fig. 13 shows the results of the sensitivity analysis at the oscillating amplitude of 10 mm, for the floating buoy. As shown, at frequencies smaller than 0.3 Hz, a small change in the measured force results in large differences in the calculated added mass.

Fig. 14 shows the damping coefficients obtained from the BEM, FVM, and experimental methods for the floating and the submerged bodies. The mean values and the standard deviations are plotted for the experimental results, as discussed in Section 3.

In general, for both bodies, the damping coefficient increases as the wave frequency increases. For the floating body, experimental results show that the damping coefficients increase slightly as the vertical

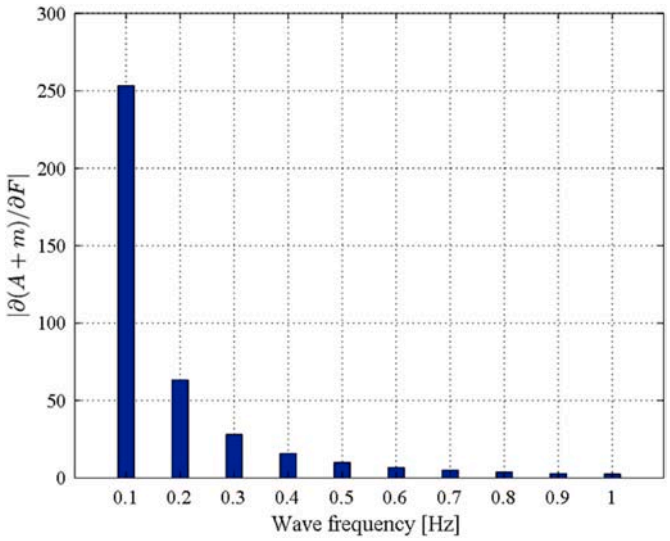

Fig. 13. Added mass sensitivity in terms of frequency.

displacement increases. However, for the submerged body, the damping coefficient is not a strong function of the wave height. Comparing the experimental and FVM results with the BEM results shows that the damping coefficients obtained by the BEM are smaller than the corresponding values obtained by the other two methods. This is due to the fact that the viscous damping is neglected in the BEM. The results also show that the differences between the damping coefficients obtained by the experimental and the FVM method compared to those obtained by the BEM method are much larger for the submerged body than for the floating body. This shows that radiation damping is dominant for the floating buoy, while viscous damping is dominant for the submerged body. The results indicate that the BEM is not a suitable method for calculating the damping coefficient of the submerged body.

In order to consider the viscosity effect for the submerged body when using the BEM method, Liang et al. [25] defined a dimensionless damping coefficient, ζ_2, for the submerged body, as:

$$\zeta_2 = \frac{b_{vis_2}}{2m_1\omega_f} \tag{38}$$

In which, b_{vis_2} is the viscous coefficient of the submerged body, m_1 is the mass of the floating body, and ω_f is the natural frequency of the floating body. They suggest choosing a value between 0.4 and 0.8 for ζ_2 and to use Eq. (38) to obtain a value for b_{vis_2} [26]. In the current study, the experimental and FVM results obtained for the damping coefficients of the submerged body are used to justify their suggestion. Fig. 15 compares the damping coefficients obtained from the experiments and the FVM methods with the corresponding values obtained when different values of ζ_2 in the range of 0.4–1 are chosen. As shown in this figure, using a value of 0.8–1 for ζ_2 in the frequency range of 0.4–1 Hz represents a reasonable estimate for the viscous damping coefficient. In this range, experimental results are relatively close to the results obtained for the suggested value for ζ_2. However, outside this range of frequency, a significant discrepancy is observed.

4.2. Diffraction test

Fig. 16 shows the wave excitation force exerted on the floating and submerged bodies, calculated by the experimental and BEM methods. In this figure, both results are also compared with the excitation force calculated using the Haskind correlation – defined as [5]:

$$F_e = \sqrt{\frac{2\rho g^3 B_j}{\omega^3}} \tag{39}$$

where, B_j is the radiation damping coefficient of the body *j*.

The forces shown at each frequency are normalized to the amplitude of the incident wave. For both bodies, the results obtained from the BEM are consistent with those of Haskind. Experimental results are also reasonably close to the BEM and Haskind results.

As shown in Fig. 16 (a), for the floating body, the wave excitation force decreases with increasing frequency, which is consistent with Haskind's correlation. Considering this equation for the floating body, the exciting force decreases as the frequency increases. On the other

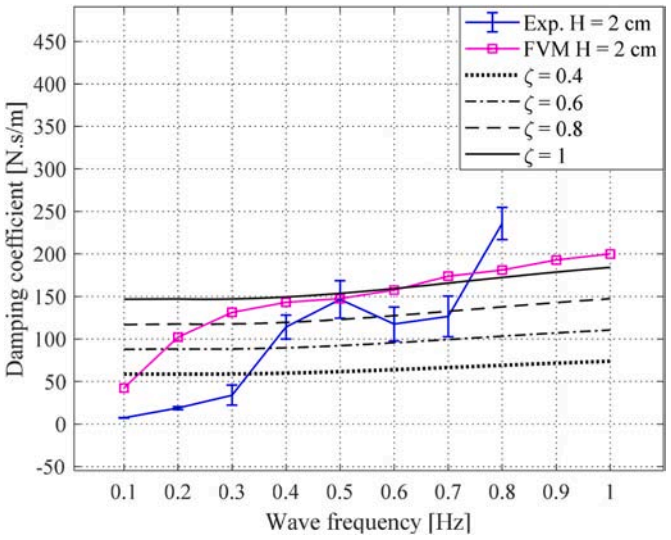

Fig. 15. Viscous damping of the submerged body calculated by dimensionless damping coefficient, ζ_2.

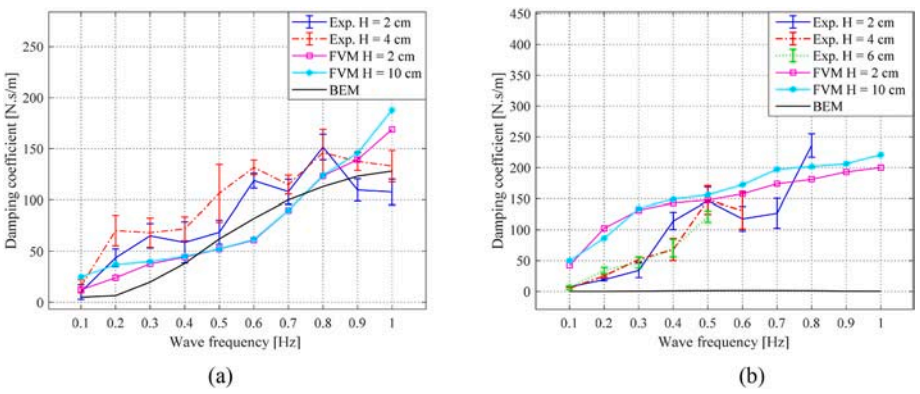

Fig. 14. Damping coefficient obtained by different methods for (a) floating buoy and (b) submerged body.

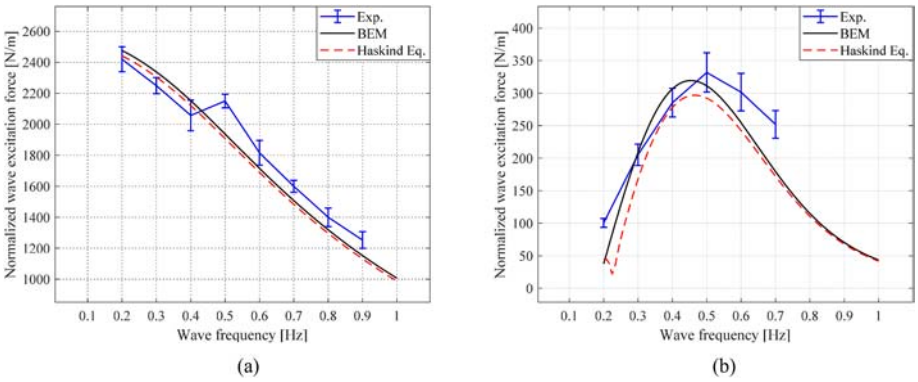

Fig. 16. Normalized wave excitation force acting on (a) the floating buoy, and (b) the submerged body. (The force is normalized by the wave height, η).

hand, by increasing the frequency, the damping coefficient B_j increases as well, see Fig. 14. Since the dominant parameter in this equation is the frequency, the exciting force decreases with increasing frequency. For the submerged body, as Fig. 16 (b) shows, the wave excitation force increases with increasing wave frequency up to 0.45 Hz. After that, it decreases. This is due to the higher increase in the radiation damping coefficient at larger frequencies.

4.3. Power absorption

Fig. 17 shows the time-averaged mechanical absorbed power of the WEC. The absorbed power is normalized to the wave amplitude, and the PTO parameters are considered to be suboptimal. Comparing the results obtained for the absorbed power by the BEM and experimental methods, one can conclude that viscous damping force has a significant effect on the absorbed power. Without considering the viscous damping, the maximum power occurs between the frequency range of 0.5–0.6 Hz (the natural frequency of the system is 0.52 Hz) and is equal to 4500 W/m^2. However, if the viscous damping is considered, the absorbed power is decreased to 1500 W/m^2.

The figure indicates that for $\zeta_2 = 1$ the calculated absorbed power agrees well with that obtained by the experimental method. This again shows that $\zeta_2 = 1$ is an appropriate estimation for the 2B-PA WECs.

4.4. Upper bound power

The upper bound absorbed power is calculated using Eqs. (25) and (26), as described in Section 2.3. The parameters in these equations can be calculated either by numerical simulations or by the experimental methods. There are two ways to calculate $\widehat{F}_{eq}$; (a) by using Eq. (6), and (b) by using the method described in Section 3.1.3.3. Fig. 18 compares the results obtained for the normalized net force $\widehat{F}_{eq}/\eta$ obtained from cases (a) and (b). On the other hand, there are three ways to calculate $\widehat{U}_{rel_{max}}$; (c) by using Eq. (23), (d) by using the experimental method described in Section 3.1.3.3, and (e) by using Eq. (24). Fig. 19 compares the normalized maximum relative velocity of two bodies, $\widehat{U}_{rel_{max}}/\eta$. In cases (c) and (d), the PTO is removed, or its impedance is set to zero ($Z_{PTO} = 0$). In case (e), the PTO maximum stroke, s_{max}, is set to 75 mm. In this case, the maximum relative velocity is obtained from Eq. (24). For the experimental cases, the tests are carried out in the frequency range of 0.3–0.9 Hz, with a frequency interval of 0.1 Hz. To increase the reliability of the results, each test is repeated three times at each frequency. For cases (a), (c), and (e), the hydrodynamic coefficients obtained by the experimental method, as described in Section 3.1.3.1, are used.

As mentioned in Section 2.3, there are two approaches to calculate the upper bound absorbed power; (i) using Eq. (25) and (ii) using Eq. (26). Depending on which parameters indicated by cases (a) to (e) are used in Eqs. (25) and (26), different values may be obtained for the upper bound absorbed power. Fig. 20 illustrates the upper bound power obtained from numerical and experimental results for various cases.

The solid black line shows the normalized upper bound power, obtained from approach (i), in which $\widehat{F}_{eq}$ and $\widehat{U}_{rel_{max}}$ are calculated numerically from *cases (a) and (c),* respectively.

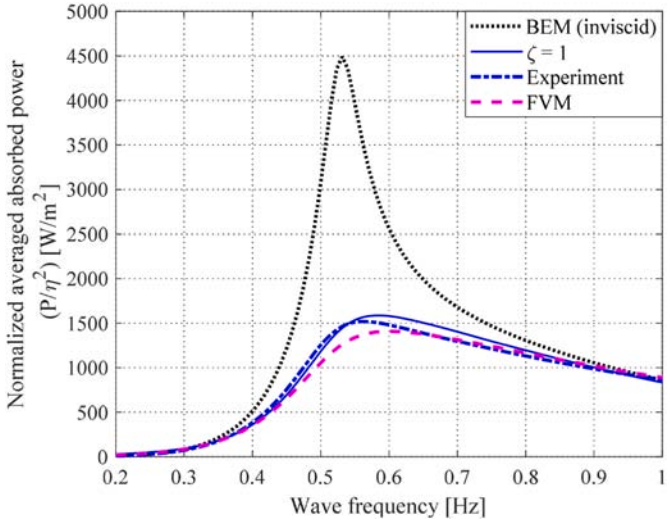

Fig. 17. Mechanical absorbed power of the WEC obtained from different methods.

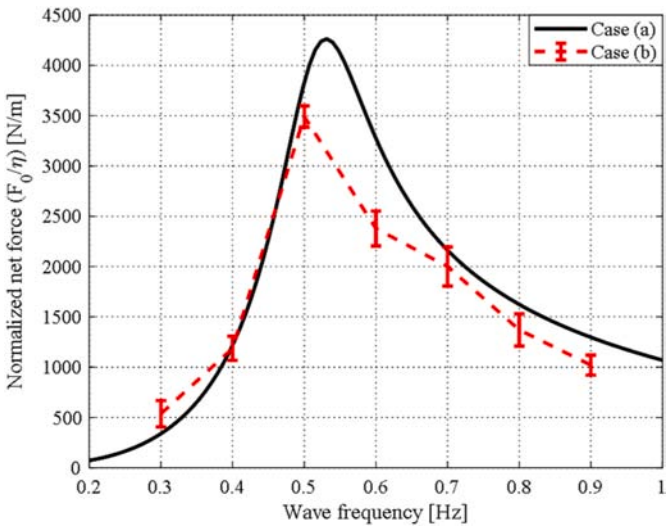

Fig. 18. The maximum possible net force.

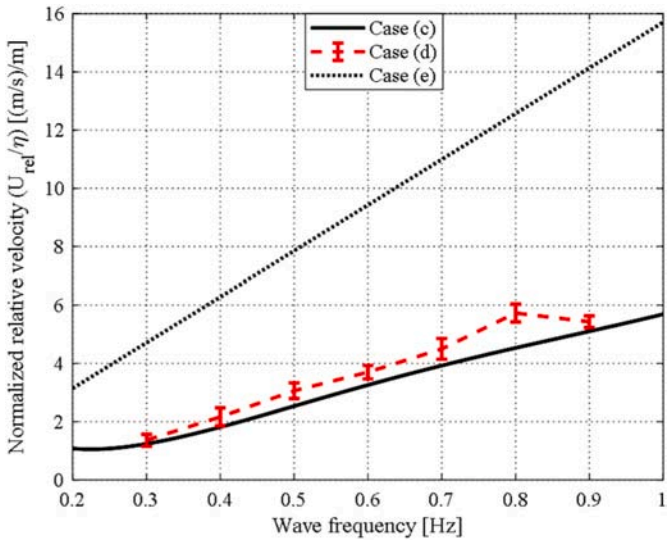

Fig. 19. The relative velocity of bodies without PTO.

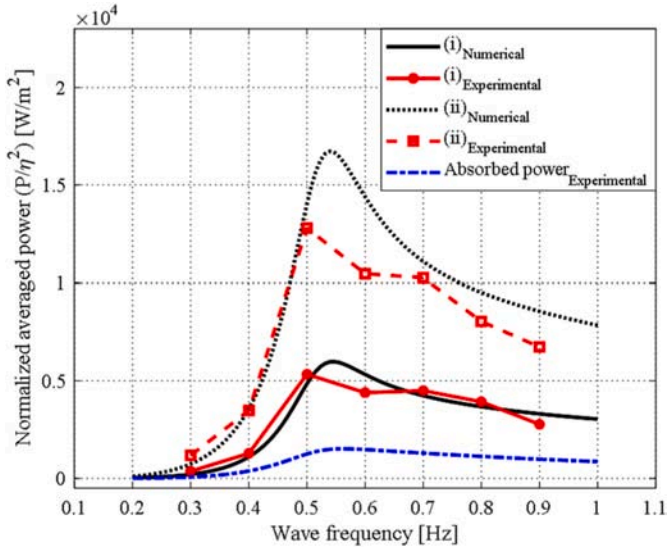

Fig. 20. The normalized averaged absorbed power and its upper bounds.

The solid red line shows the normalized upper bound power, obtained from approach (i), in which $\widehat{F}_{eq}$ and $\widehat{U}_{rel_{max}}$ are calculated experimentally from *cases (b) and (d),* respectively.

The dotted black line shows the normalized upper bound power, obtained from approach (ii), in which $\widehat{F}_{eq}$ and $\widehat{U}_{rel_{max}}$ are calculated numerically from *cases (a) and (e),* respectively.

The dashed red line shows the normalized upper bound power, obtained from approach (ii), in which $\widehat{F}_{eq}$ and $\widehat{U}_{rel_{max}}$ are calculated experimentally from *cases (b) and (e),* respectively.

The dashed blue line represents the time-averaged absorbed power calculated from Eq. (9).

The results of the two approaches for the upper bound on power prove that PTO stroke does not imply any restrictions on power absorption, and the value of 75 mm is an acceptable range for PTO stroke. Fig. 20 shows that the maximum upper bound power based on the approach (i), the dominant approach, occurs in the frequency range of 0.5–0.6 Hz. The maximum values are 5972 and 5320 W/m^2 for the numerical and the experimental results, respectively. The peak of absorbed power for the fabricated WEC is around 1500 W/m^2, which is 27% of the upper bound at the corresponding frequency.

5. Conclusions

This study is conducted to estimate the amount of mechanical power absorbed by a 2B-PA WEC oscillating in regular waves. Three methods – namely the BEM, the FVM, and the experimental method – are used to calculate the bodies hydrodynamic coefficients and wave excitation force. A vertical oscillating mechanism, equipped with the measuring instruments, is implemented to be able to run different experiments in order to calculate and validate the hydrodynamic coefficients. The upper bound of the absorbed power is also calculated using two approaches – both numerically and experimentally.

Comparing the numerical and experimental results reveals that the BEM is not a suitable tool to estimate the absorbed power. Although the BEM is a fast and economic method, it is not able to consider the viscosity – and this study shows that the viscosity has a strong effect on the absorbed power. The current study also proves that FVM is a suitable tool for calculating the damping coefficient because its results are consistent with the experimental data. A comparison of the results of the three methods for calculating the damping coefficient shows that for the floating buoy, the radiation damping is the dominant part of the damping coefficient, while the viscous damping is negligible. However, the viscous damping is the main part of the submerged body drag. For the 2B-PA WECs, which have the same geometry as the one presented in this study, it is recommended – since the viscous damping is a shape factor function – to choose ζ_2 in the range of 0.8–1 to estimate the viscous damping of the submerged body. The upper bound power study reveals that the fabricated WEC is able to harvest 27% of the maximum available power.

CRediT authorship contribution statement

Amir Rahimi: Conceptualization, Methodology, Software, Visualization, Validation, Writing – original draft. **Saeed Rezaei:** Conceptualization, Investigation, Validation, Writing – original draft. **Jamshid Parvizian:** Project administration, Writing – review & editing, Funding acquisition. **Shahriar Mansourzadeh:** Supervision, Writing – review & editing, Validation. **Jorrid Lund:** Software, Validation. **Radhouane Hssini:** Software, Investigation. **Alexander Düster:** Project administration, Writing – review & editing, Funding acquisition.

Declaration of competing interest

The authors declare that they have no known competing financial interests or personal relationships that could have appeared to influence the work reported in this paper.

Data availability

Data will be made available on request.

Acknowledgment

This work is the result of an institutional partnership being supported by the Alexander von Humboldt Foundation. This support is gratefully acknowledged.

Appendix A

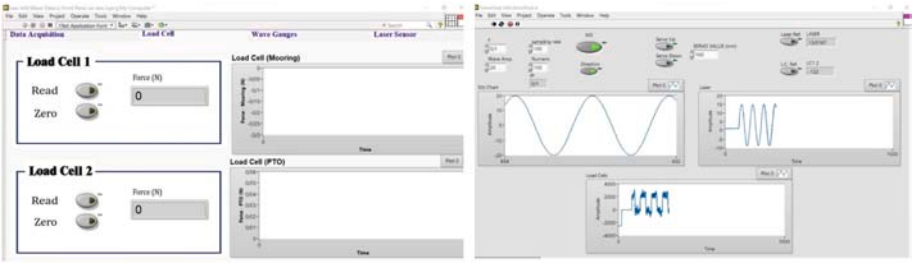

Fig. A1. The graphical user interface (GUI) used for data acquisition in VOM system.

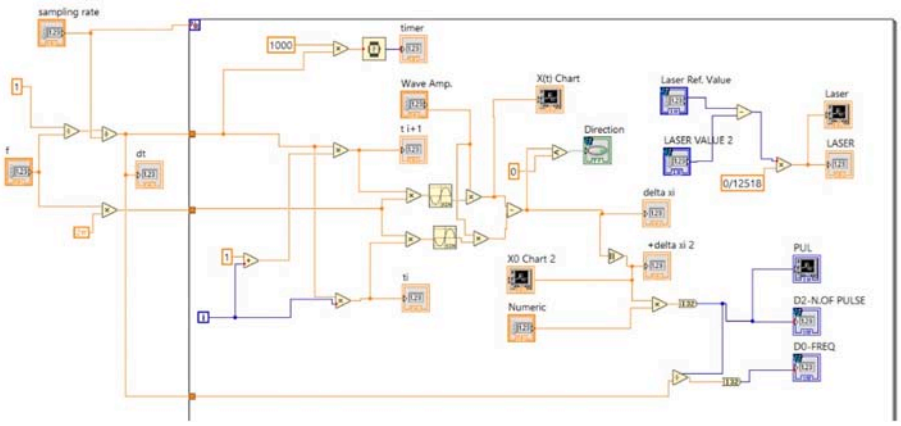

Fig. A2. The core of the LabView block diagram used for the VOM system.

References

[1] J. Falnes, A review of wave-energy extraction, Mar. Struct. 20 (4) (2007) 185–201.
[2] B. Drew, A.R. Plummer, M.N. Sahinkaya, *Rev. Wave Energy converter Technol.. Proc. Ins. Mech. Eng. Part A*: J. Power Energy 223 (8) (2009) 887–902.
[3] A.F.d.O. Falcão, Wave energy utilization: a review of the technologies, Renew. Sustain. Energy Rev. 14 (3) (2010) 899–918.
[4] E. Al Shami, R. Zhang, X. Wang, Point absorber wave energy harvesters: a review of recent developments, Energies 12 (1) (2019) 47.
[5] W.J. Pierson, Falnes Johannes, Waves Ocean, Oscillating Systems, Linear interactions including wave energy extraction, Mar. Technol. SNAME News 39 (4) (2002).
[6] J. Falnes, Wave-energy conversion through relative motion between two single-mode oscillating bodies, J. Offshore Mech. Arctic Eng. 121 (1999) 32–38.
[7] E. Al Shami, et al., A parameter study and optimization of two body wave energy converters, Renew. Energy 131 (2019) 1–13.
[8] A.S. Zurkinden, et al., Non-linear numerical modeling and experimental testing of a point absorber wave energy converter, Ocean Eng. 78 (2014) 11–21.
[9] B. Bosma, et al., Wave tank testing and model validation of an autonomous wave energy converter, Energies 8 (8) (2015) 8857–8872.
[10] G. Bacelli, et al., Wave tank and bench-top control testing of a wave energy converter, Appl. Ocean Res. 86 (2019) 351–366.
[11] T.D. Dang, C.B. Phan, K.K. Ahn, Modeling and experimental investigation on performance of a wave energy converter with mechanical power take-off, Int. J. Precis. Eng. Manufac-Green Technol. 6 (4) (2019) 751–768.
[12] D. Martin, et al., Numerical analysis and wave tank validation on the optimal design of a two-body wave energy converter, Renew. Energy 145 (2020) 632–641.
[13] S. Wu, Y. Liu, J. Qin, Experimental analyses of two-body wave energy converters with hydraulic power take-off damping in regular and irregular waves, IET Renew. Power Gener. (2021).
[14] K. Edwards, M. Mekhiche, Ocean power technologies powerbuoy®: system-level design, development and validation methodology. (2014).
[15] J. Weber, et al., Wavebob—research & development network and tools in the context of systems engineering, in: Proc. Eighth European Wave and Tidal Energy Conference, Uppsala, Sweden, 2009.
[16] A. Weinstein, et al., AquaBuOY-the Offshore Wave Energy Converter Numerical Modeling and Optimization, in: Oceans 2003. Celebrating the Past... Teaming toward the Future (IEEE Cat. No. 03CH37492), IEEE, 2003.
[17] R. Yemm, et al., *Pelamis: experience from concept to connection.* Philosophical transactions of the royal society A: mathematical, Phys. Eng. Sci. 2012 (1959) 365–380, 370.
[18] E. Callaway, To catch a wave: ocean wave energy is trying to break into the renewable-energy market, but many challenges remain, Nature 450 (7167) (2007) 156–160.
[19] J. Morim, et al., A review of wave energy estimates for nearshore shelf waters off Australia, Int. J. Mar. Energy 7 (2014) 57–70.
[20] S. Illesinghe, et al., Idealized design parameters of Wave Energy Converters in a range of ocean wave climates, Int. J. Mar. Energy 19 (2017) 55–69.
[21] J. Engström, et al., A resonant two body system for a point absorbing wave energy converter with direct-driven linear generator, J. Appl. Phys. 110 (12) (2011) 124904.
[22] S.R. Massel, Ocean waves breaking and marine aerosol fluxes 38 (2007). Springer Science & Business Media.
[23] E. Al Shami, X. Wang, X. Ji, A study of the effects of increasing the degrees of freedom of a point-absorber wave energy converter on its harvesting performance, Mech. Syst. Signal Process. 133 (2019) 106281.
[24] S. Bozzi, et al., Modeling of a point absorber for energy conversion in Italian seas, Energies 6 (6) (2013) 3033–3051.
[25] C. Liang, L. Zuo, On the dynamics and design of a two-body wave energy converter, Renew. Energy 101 (2017) 265–274.
[26] S.J. Beatty, et al., Experimental and numerical comparisons of self-reacting point absorber wave energy converters in regular waves, Ocean Eng. 104 (2015) 370–386.
[27] J.J. Stoker, Water waves: The mathematical theory with applications 36, 2011. John Wiley & Sons.
[28] S.J. Beatty, et al., Experimental and numerical comparisons of self-reacting point absorber wave energy converters in irregular waves, Ocean Eng. 173 (2019) 716–731.
[29] Ocean power technologies, last accessed data, 2021 https://oceanpowertechnologies.com/.
[30] S. Jin, R.J. Patton, B. Guo, Viscosity effect on a point absorber wave energy converter hydrodynamics validated by simulation and experiment, Renew. Energy 129 (2018) 500–512.
[31] Z.f. Chen, et al., Geometrical evaluation on the viscous effect of point-absorber wave-energy converters, China Ocean Eng. 32 (4) (2018) 443–452.
[32] E. Al Shami, Z. Wang, X. Wang, Non-linear dynamic simulations of two-body wave energy converters via identification of viscous drag coefficients of different shapes of the submerged body based on numerical wave tank CFD simulation, Renew. Energy 179 (2021) 983–997.
[33] S. Rezaei, et al., Dimensional optimization of a two-body Wave energy converter using response surface methodology, Ocean Eng. 261 (2022) 112186.
[34] Inc ANSYS, AQWA theory manual. Canonsburg, PA 15317 (2017).

[35] Christopher J. Greenshields, "OpenFOAM user guide." OpenFOAM foundation Ltd, version 3, no 1, 2015, p. 47.
[36] J.H. Ferziger, M. Perić, R.L. Street, Computational Methods for Fluid Dynamics 3, Springer, 2002.
[37] Radhouane Hssini, Optimization of Wave Energy Converter Parameters Using Partitioned Fluid-Structure Interaction Simulations, in: Master Thesis, Hamburg University of Technology, Sept, 2021.
[38] A.R. Taeid, Numerical Simulation of A Two-Body Point Absorber Wave Energy Converter, in: Master Thesis, Isfahan University of Technology, Sept, 2022.
[39] J. Kodosky, LabVIEW, in: Proceedings of the ACM on Programming Languages 4, 2020, pp. 1–54.
[40] L. Tao, S. Cai, Heave motion suppression of a Spar with a heave plate, Ocean Eng. 31 (5–6) (2004) 669–692.